

ON THE DIFFERENCE OF TORUS GEOMETRY BETWEEN HIDDEN AND NON-HIDDEN BROAD LINE ACTIVE GALACTIC NUCLEI

KOHEI ICHIKAWA^{1,14}, CHRISTOPHER PACKHAM², CRISTINA RAMOS ALMEIDA^{3,4,15}, ANDRÉS ASENSIO RAMOS^{3,4}, ALMUDENA ALONSO-HERRERO^{5,16}, OMAIRA GONZÁLEZ-MARTÍN^{3,4}, ENRIQUE LOPEZ-RODRIGUEZ², YOSHIHIRO UEDA¹, TANIO DÍAZ-SANTOS^{6,7}, MOSHE ELITZUR⁸, SEBASTIAN F. HÖNIG^{9,15}, MASATOSHI IMANISHI¹⁰, NANCY A. LEVENSON¹¹, RACHEL E. MASON¹², ERIC S. PERLMAN¹³, AND CRYSTAL D. ALSIP²

¹ Department of Astronomy, Kyoto University, Kitashirakawa-Oiwake-cho, Sakyo-ku, Kyoto 606-8502, Japan

² Department of Physics and Astronomy, University of Texas at San Antonio, One UTSA Circle, San Antonio, TX 78249, USA

³ Instituto de Astrofísica de Canarias, C/Vía Láctea, s/n, E-38205 La Laguna, Tenerife, Spain

⁴ Departamento de Astrofísica, Universidad de La Laguna, E-38205 La Laguna, Tenerife, Spain

⁵ Instituto de Física de Cantabria, CSIC-Universidad de Cantabria, 39005 Santander, Spain

⁶ Spitzer Science Center, California Institute of Technology, MS 220-6, Pasadena, CA 91125, USA

⁷ Nucleo de Astronomía de la Facultad de Ingeniería, Universidad Diego Portales, Av. Ejercito Libertador 441, Santiago, Chile

⁸ Department of Physics and Astronomy, University of Kentucky, Lexington, KY 40506-0055, USA

⁹ School of Physics and Astronomy, University of Southampton, Southampton SO17 1BJ, UK

¹⁰ Subaru Telescope, 650 North A'ohoku Place, Hilo, HI 96720, USA

¹¹ Gemini Observatory, Southern Operations Center, c/o AURA, Casilla 603, La Serena, Chile

¹² Gemini Observatory, Northern Operations Center, 670 N. A'ohoku Place, Hilo, HI 96720, USA and

¹³ Department of Physics and Space Sciences, 150 W. University Blvd., Florida Institute of Technology, Melbourne, FL 32901, USA

Draft version November 10, 2021

ABSTRACT

We present results from the fitting of infrared (IR) spectral energy distributions of 21 active galactic nuclei (AGN) with clumpy torus models. We compiled high spatial resolution (~ 0.3 – 0.7 arcsec) mid-IR N -band spectroscopy, Q -band imaging and nuclear near- and mid-IR photometry from the literature. Combining these nuclear near- and mid-IR observations, far-IR photometry and clumpy torus models, enables us to put constraints on the torus properties and geometry. We divide the sample into three types according to the broad line region (BLR) properties; type-1s, type-2s with scattered or hidden broad line region (HBLR) previously observed, and type-2s without any published HBLR signature (NHBLR). Comparing the torus model parameters gives us the first quantitative torus geometrical view for each subgroup. We find that NHBLR AGN have smaller torus opening angles and larger covering factors than those of HBLR AGN. This suggests that the chance to observe scattered (polarized) flux from the BLR in NHBLR could be reduced by the dual effects of (a) less scattering medium due to the reduced scattering volume given the small torus opening angle and (b) the increased torus obscuration between the observer and the scattering region. These effects give a reasonable explanation for the lack of observed HBLR in some type-2 AGN.

Subject headings: galaxies: active — galaxies: nuclei — infrared: galaxies

1. INTRODUCTION

While active galactic nuclei (AGN) present a variety of observational characteristics, the unified model for AGN proposes the ubiquitous presence of an obscuring torus around their central engines, and that all AGN are fundamentally the same (Antonucci 1993). This optically and geometrically thick torus produces the effect of a line of sight viewing angle dependency. Type-1 AGN are observed with the direct view of fast moving material close to the supermassive black hole (SMBH), resulting in broad emission lines in their spectra, while type-2 AGN are observed from an edge-on view and the torus blocks the broad emission line region (BLR) component from our line of sight. The most compelling evidence of the unified model was the detection of polarized broad emission lines (PBLs) in type-2 AGN (e.g., Antonucci & Miller 1985). Further evidence supporting the unified model comes from infrared (IR) obser-

vations of several type-2 AGN showing the existence of obscured/hidden broad line regions (HBLRs) detectable only with dust penetrating infrared observations (e.g., Blanco et al. 1990; Nagar et al. 2002; Reunanen et al. 2003; Ramos Almeida et al. 2008).

Against the fact that the observations generally support the unified model, there is the question of why some, but not all, type-2 AGN do not show any observational signs of PBLs. Tran (2001, 2003) and Moran et al. (2001) found that only 30–50% of type-2 AGN show PBLs. Some studies have advocated that the non-detection of a PBL is due to genuine lack of a BLR (e.g., Tran et al. 2011). Others have suggested that the non-detection is due to obscuration effects, rendering the detection of PBLs as difficult or impossible, even with deep near-IR (NIR) spectro-polarimetric observations (Alexander 2001). Using a statistically complete *IRAS* 60 μ m selected type-2 AGN catalog, Heisler et al. (1997) investigated the relationship between the detectability of PBLs and IR color as an indicator of the torus inclination angle. They showed that only AGN with a low torus inclination angle have high detection rate of PBLs compared to those with high inclinations. This result strongly suggests that

ichikawa@kustastro.kyoto-u.ac.jp

¹⁴ JSPS research fellow (DC1), Japan

¹⁵ Marie Curie fellow

¹⁶ Visiting Professor, Department of Physics and Astronomy, University of Texas at San Antonio

PBLs could be obscured when there is an edge-on view through the torus and/or nuclear obscuration in the host galaxies. In addition to the optical spectro-polarimetry, X-ray observations suggest that there is a weak evidence showing different absorption in two types of type-2 AGN. Gu et al. (2001) found that the AGN with PBL have slightly lower column density (N_{H}) than those without PBL. Similarly, Lumsden et al. (2004) showed that the detection rate of PBL decreases as a function of N_{H} , suggesting that the absorption effect by dusty torus could play a role on the detectability of PBL in AGN.

To understand the role of the obscuration by the torus in type-2 AGN and the detectability of PBLs, knowing the torus geometry and properties is crucial. In recent years much progress has been made toward understanding the torus geometrical structure. Thanks to the improvement of computing power, more physically realistic torus models assuming ‘‘clumpy’’ distributions (called clumpy torus models) have been coded by several authors (Nenkova et al. 2002, 2008a,b; Hönig et al. 2006; Schartmann et al. 2008; Hönig & Kishimoto 2010; Stalevski et al. 2012). These models readily reproduce high spatial resolution nuclear NIR to mid-IR (MIR) spectral energy distributions (SEDs) and spectra of AGN with a compact torus of < 10 pc radius (e.g., Ramos Almeida et al. 2009, 2011a; Nikutta et al. 2009; Alonso-Herrero et al. 2011; Hönig et al. 2011; Lira et al. 2013). On the other hand, traditional smooth torus models (Pier & Krolik 1992, 1993; Efstathiou & Rowan-Robinson 1995) had difficulties to describe the variety of nuclear SEDs of nearby AGN (e.g., Alonso-Herrero et al. 2003; Gandhi et al. 2009; Asmus et al. 2011; Ichikawa et al. 2012a). Still, the true torus morphology remains far from being conclusively determined until future observations resolve the torus. Both smooth and clumpy torus models have degeneracies, and from SED-fitting alone is not possible to choose one or the other (see Feltre et al. 2012, for a comparison between smooth and clumpy torus models).

In this paper, under the assumption that the torus follows a clumpy distribution of dust, which we consider more realistic in principle, we discuss how the precise modeled torus morphology plays a key role in the probability of the detection of PBL by fitting clumpy torus models to our series of IR SEDs. We use 21 high spatial resolution MIR spectra in combination with NIR to far-IR (FIR) photometry, constituting one of the largest compilations of nuclear IR SEDs of AGN in the local universe. These SEDs afforded by 8 m class telescopes minimize contamination of the MIR torus spectra from surrounded diffuse MIR emission from warm dust and/or starformation region emission, and hence we are able to construct the highest fidelity torus SED. Therefore we can probe the detectability of the PBL with the least amount of host galaxy contaminations than ever before. The luminosity dependence of the torus morphology will be discussed in a forthcoming paper (Ichikawa et al. in prep.).

2. OBSERVATIONS

2.1. The Sample

Our principal motivation in this study is to investigate whether the torus model morphology plays a major role in the chance of PBL detections. To achieve this goal, we

compiled the nearby AGN sources from the MIR samples of González-Martín et al. (2013) (21 sources) and Alonso-Herrero et al. (2011) (13 sources) as both samples already compiled the currently available data set of ground-based N band spectroscopy. Of the 34 sources, five are in common in both samples, therefore the total number is 29 sources. We further set the criteria for survey inclusion that the objects must have at least one high spatial resolution NIR (1–5 μm) measurement, as the NIR bands significantly help to constrain the torus parameters (Ramos Almeida et al. 2014). 22 out of 29 sources fulfilled this criterion. We also removed NGC 1808 from this study as controversy remains to whether it hosts AGN or ultra-luminous X-ray sources in the galactic center due to the low X-ray luminosity $\log L_{2-10 \text{ keV}} = 40.4 \text{ erg s}^{-1}$ (Scarrott et al. 1993; Jiménez-Bailón et al. 2005). We summarize the properties of the 21 sources in Table 1.

Our sample spans AGN bolometric luminosities taken from the literature ($L_{\text{bol}}^{\text{(lit)}}$) in the range $\log L_{\text{bol}}^{\text{(lit)}} = 42.7\text{--}45.1 \text{ erg s}^{-1}$ (see Table 1), with a mean value of 44.0 erg s^{-1} . This value is fairly consistent with that of magnitude-limited Seyfert catalogs (Maiolino & Rieke 1995; Ho et al. 1997). This suggests that our sample could be representative of AGN and their tori in the local universe, although the sample is not complete.

2.2. New Observations

We obtained N (Si2 filter; the central wavelength with $\lambda_c = 8.73 \mu\text{m}$ and 50% cutoff range of $\Delta\lambda = 0.39 \mu\text{m}$) and Q (Qa filter; $\lambda_c = 18.06 \mu\text{m}$ and $\Delta\lambda = 0.76 \mu\text{m}$) band imaging data of NGC 5135 and NGC 5643, observed by T-ReCS (Program ID GS-2012A-Q-43, PI: Nancy Levenson). The standard MIR chop-nod technique was performed for the observations. The data reduction was made by using REDCAN (González-Martín et al. 2013).

2.3. Published Data from the Literature

We collected the estimated values of the nuclear NIR to MIR emission when available. We compiled nuclear NIR data from both ground- and space-based telescopes such as VLT/NACO and *HST*/NICMOS. The only exception is the galaxy NGC 5728, whose only NIR flux is from 2MASS (Peng et al. 2006), which we use as an upper limit. Information about the NIR fluxes used here is compiled in Table 2 (columns 2-6).

In order to further reduce the parameters space at longer wavelengths, we used the *Spitzer*/IRS 30 μm continuum fluxes reported by Deo et al. (2009) as upper limits in our fits. We do that because the star formation component can be important at 20–30 μm , and beyond 30 μm completely overwhelms the AGN torus emission in most cases (Netzer et al. 2007) at the spatial resolutions afforded by *Spitzer*. We only consider the *Spitzer* 30 μm photometry as data points, and also included the *Spitzer*/IRS spectroscopy when the AGN spectral turnover at 20–30 μm is clearly seen in the IRS spectra. This feature suggests that the torus emission is dominant even in the large aperture data from *Spitzer* (Alonso-Herrero et al. 2012b; Hönig et al. 2014). Only two sources fulfilled the criterion (IC 4329A and MCG -5-23-16). For those galaxies, we also collected available *Herschel*/PACS data. All the FIR flux information is

TABLE 1
PROPERTIES OF THE SAMPLE

Name (1)	z (2)	d (3)	Slit/Size (4)	Type (5)	Group (6)	N_H (7)	$\log L_{\text{bol}}^{(\text{lit})}$ (8)	b/a (9)	A_V (10)	i (11)	Ref (12)
NGC 1365	0.0055	18	0.35/31	Sy1.8	Type-1	23.6	42.9	0.5	<5	...	(A1,B1,B1,...)
NGC 4151	0.0033	13	0.36/23	Sy1.5	Type-1	22.8	43.7	0.71	(A9,A9,...)
IC 4329A	0.016	65	0.75/240	Sy1.2	Type-1	21.8	43.6	0.28	(A10,A9,...)
NGC 7469	0.016	66	0.75/240	Sy1	Type-1	20.7	45.1	0.72	(A9,A9,...)
NGC 1068	0.0038	15	0.36/26	Sy2	HBLR	> 25	45.0	0.85	...	60–90	(A2,A9,...)
NGC 2110	0.0078	31	0.36/54	Sy2	HBLR	22.5	43.9	0.74	5	40	(A9,A9,A9,A9)
MCG -5-23-16	0.0085	34	0.75/120	Sy2	HBLR	22.2	44.4	0.46	>6	53	(A9,A9,A9,A9)
NGC 3081	0.008	32	0.65/100	Sy2	HBLR	23.9	43.8	0.8	(A3,B2,...)
NGC 3227	0.0039	17	0.75/62	Sy2	HBLR	22.2	43.4	0.68	(A11,A9,...)
Circinus	0.0014	4	0.60/12	Sy2	HBLR	24.6	43.6	0.44	9	60–90	(A8,A9,A9,A9)
NGC 5506	0.0062	25	0.36/44	Sy2	HBLR	22.4	44.2	0.30	≥ 11	40	(A9,A9,A9,A9)
IC 5063	0.011	46	0.67/150	Sy2	HBLR	23.3	44.5	0.68	7	...	(A2,A9,A9,...)
NGC 7582	0.0053	21	0.75/76	Sy2	HBLR	22.7	43.3	0.42	8,13	...	(A9,A9,A9,...)
NGC 7674	0.029	118	0.75/430	Sy2	HBLR	>25	45.0	0.91	$\sim 3-5$...	(A9,A9,A9,...)
NGC 1386	0.0029	11	0.31/17	Sy2	NHBLR	>25.0	42.9	0.4	...	65,85	(A2,B2,...,C1)
NGC 3281	0.011	43	0.35/73	Sy2	NHBLR	24.3	44.6	0.4	(A4,B1,...)
Cen A	0.0018	3	0.65/11	Sy2	NHBLR	23.7	44.0	0.4	14.0	...	(A5,B2,A9,...)
NGC 5135	0.014	59	0.70/200	Sy2	NHBLR	>25.0	44.4	0.7	(A2,B2,...)
NGC 5643	0.004	16	0.35/29	Sy2	NHBLR	23.8	42.7	0.9	(A6,B5,...)
NGC 5728	0.0094	40	0.35/69	Sy2	NHBLR	23.6	44.5	0.6	(A7,B6,...)
NGC 7172	0.0087	35	0.36/61	Sy2	NHBLR	22.9	43.8	0.46	(A2,A9,...)

NOTE. — Sample properties. The sample is divided into three subgroups with type-1/HBLR/NHBLR respectively from top to bottom. (1) object name; (2) redshift; (3) luminosity distance (Mpc) gathered from literature for the case of nearby sources. Within the sample of González-Martín et al. (2013), for NGC 1365, NGC 1386, NGC 1808, NGC3081, NGC 3281, and Cen A, the values of distance to the galaxies have been taken from Ramos Almeida et al. (2009). For NGC 5643, the distance has been taken from Guainazzi et al. (2004). For the sample of Alonso-Herrero et al. (2011), we gathered them from Alonso-Herrero et al. (2011). For the other sources, we calculated the distances by using cosmological parameter $H_0 = 75 \text{ km s}^{-1} \text{ Mpc}^{-1}$; (4) slit width (arcsec) / physical size (pc); (5) Seyfert class of AGN. (6) Sub group of AGN. Type-1 represents type-1 AGN (Sy 1 to Sy 1.9) based on optical spectroscopy. HBLR represents type-2 (Sy2) AGN with hidden broad line region signs, and NHBLR represents type-2 AGN without any published hidden broad line regions signs. (7) hydrogen column density; (8) logarithm of bolometric luminosity (erg/s) which is taken from González-Martín et al. (2013); Alonso-Herrero et al. (2011). We use a typical bolometric correction of 20 (Elvis et al. 1994). (9) The axial ratio; the ratio of the minor to major axis of the host galaxies. All information is taken from González-Martín et al. (2013); (10) Foreground extinction in the unit of mag; (11) inclination angle of the torus. Levenson et al. (2006) derives the viewing angle of accretion disk of NGC 1386 and we here assume that the accretion disk and the torus are located in the same plane; (12) References of column (6), (7), (10), and (11). “...” denotes no reference.

References. (A1) Alonso-Herrero et al. (2012a); (A2) Tran (2001); (A3) Moran et al. (2000); (A4) Nicastrò et al. (2003); (A5) Alexander et al. (1999); (A6) Gu et al. (2001); (A7) Tran (2003); (A8) Wang & Zhang (2007); (A9) Alonso-Herrero et al. (2011); (A10) Véron-Cetty & Véron (2006); (A11) Imanishi (2002); (B1) Tueller et al. (2008); (B2) Marinucci et al. (2012); (B3) Brightman & Nandra (2011); (B4) Itoh et al. (2008); (B5) Guainazzi et al. (2004); (B6) Goulding et al. (2012); (C1) Levenson et al. (2006)

tabulated in column 9 to 11 in Table 2.

The errors were estimated using the prescription given by Alonso-Herrero et al. (2012a). For the NACO AO observations, we used 20% in J band and 15% in the $HKLM$ band. For the other ground-based observation data, we applied 30% for J band, 25% for H and K band, and 20% for the L band. These errors include the photometric error, the background subtraction uncertainty, and the uncertainty from estimating the unresolved flux. M band fluxes were always used as upper limits due to the difficulties of estimating the unresolved component. For the NICMOS observations, we used 20% for the J band, 20% for the H and K band. For the N and Q band, we use 15% and 25% errors, respectively.

2.4. Subsample

To examine the torus model properties of different AGN populations, we divide the sample into subgroups based on whether or not the source has HBLR signs in previously published observations. We first divide the sample into type-1 and type-2 AGN. Although Seyfert 1.8/1.9 are very ambiguous objects (e.g., see Elitzur et al. 2014, for the details), here we define type-1 as AGN which have at least one broad emission lines in their op-

tical spectra. Therefore, we consider Seyfert 1 to 1.9 as type-1 AGN and Seyfert 2 as type-2 AGN. Next, we divide the type-2 AGN into those with any published polarized BLR detections in the optical and/or in the NIR (HBLR) and those without (non-HBLR; hereafter NHBLR). We use Marin (2014), who compiled almost all the previously published polarization information of nearby AGN. These spectro-polarimetric data are taken from several large surveys including the infrared-selected sample of Heisler et al. (1997), the FIR flux limited sample of Lumsden et al. (2001), the distance-limited sample of Moran et al. (2000, 2002), and the heterogeneous optical- and MIR selected sample of Tran (2001, 2003). Mainly the spectro-polarimetric observations were conducted with small or medium size telescopes (up to 4 m-class), while only NGC 3081 has been confirmed to have HBLR features with the Keck 10 m telescope (Moran et al. 2000). Therefore, we should note that some HBLR AGN could contaminate the subgroup of NHBLR in the cases where the BLR is below the signal-to-noise afforded by the 4 m class telescope observations (see Ramos Almeida et al., in prep.). Some sources have currently no published spectro-polarimetric data, but have clear broad emission lines in NIR wavelengths. These

TABLE 2
 LIST OF PHOTOMETRY

Name (1)	J (2)	H (3)	K (4)	L (5)	M (6)	N (7)	Q (8)	$30\ \mu\text{m}$ (9)	$70\ \mu\text{m}$ (10)	$160\ \mu\text{m}$ (11)	Ref (12)
Type-1											
NGC 1365	...	8.3 ± 0.83	203 ± 30.0	818 ± 204	< 12.3	(A1,B1)
NGC 4151	69 ± 14	104 ± 10.4	178 ± 17.8	< 325	...	1320 ± 198	3200 ± 800	< 3.64	(A7,A7)
IC 4329A	...	50.0 ± 8.0	102 ± 10	< 210	...	1014 ± 150	...	1.52 ± 0.015	< 1.79	< 0.97	(A7,A7)
NGC 7469	16 ± 3.2	40 ± 4.0	68 ± 6.8	< 84	...	506 ± 76	1350 ± 340	(A7,A7)
HBLR											
NGC 1068	9.8 ± 2.0	98.0 ± 15.0	445 ± 100	920 ± 140	2270 ± 340	10000 ± 1500	21800 ± 5400	(A7,A7)
NGC 2110	< 33.0	< 198	294 ± 44	561 ± 140	< 0.8	(A7,A7)
MCG -5-23-16	1.1 ± 0.33	3.7 ± 0.93	10.7 ± 2.7	79.5 ± 16.0	< 139.4	633 ± 95	1450 ± 360	...	< 1.45	< 0.45	(A7,A7)
NGC 3081	...	0.22 ± 0.04	83 ± 12.5	231 ± 57.8	< 1.10	(A2,B1)
NGC 3227	...	11 ± 1.1	23 ± 2.3	< 47.0	...	320 ± 48	1100 ± 275	< 1.76	(A7,A7)
Circinus	< 1.60	4.77 ± 0.72	19 ± 2.9	380 ± 57	1900 ± 285	5600 ± 840	12800 ± 3200	(A7,A7)
NGC 5506	13 ± 3.0	53 ± 8.0	80 ± 12	290 ± 44	< 530	900 ± 135	2200 ± 550	< 4.05	(A7,A7)
IC 5063	...	0.3 ± 0.1	4.8 ± 1.0	925 ± 139	...	< 3.89	(A7,A7)
NGC 7582	...	11.0 ± 1.6	18.0 ± 2.7	96.0 ± 14.4	141 ± 21	384 ± 57	527 ± 132	(A7,A7)
NGC 7674	1.25 ± 0.25	5.0 ± 0.5	12.3 ± 3.1	53.0 ± 11.0	< 108	518 ± 78	...	< 1.83	(A7,A7)
NHBLR											
NGC 1386	...	0.2 ± 0.04	147 ± 22.1	457 ± 114	< 1.58	(A2,B1)
NGC 3281	...	1.3 ± 0.33	7.7 ± 1.93	103 ± 20.6	< 207	355 ± 53.3	1110 ± 278	(A4,B1)
Cen A	1.3 ± 0.26	4.5 ± 0.68	34 ± 5.1	200 ± 30	...	710 ± 107	2630 ± 658	(A5,B1)
NGC 5135	< 0.72	0.66 ± 0.07	56.36 ± 8.454	218.92 ± 54.73	< 3.03	(A2;A6, B2)
NGC 5643	...	< 1.7	101.31 ± 15.17	883.2 ± 220.8	(A2,B2)
NGC 5728	< 7.1	25 ± 3.75	184 ± 46	(A6,B1)
NGC 7172	...	< 0.4	3.4 ± 0.86	30 ± 6	< 61.4	165 ± 30	...	< 0.98	(A7,A7)

NOTE. — NIR to FIR fluxes used as inputs for BAYESCLUMPY. Units are in mJy for columns 2 to 8, and in Jy for columns 9 to 11. Column 9 corresponds to *Spitzer*/IRS $30\ \mu\text{m}$ continuum fluxes from Deo et al. (2009), which are used as upper limits in the fits. Columns 10 and 11 list the *Herschel*/PACS photometry from Meléndez et al. (2014) and are also used as upper limits. “...” represents no flux information. The references from NIR to MIR band fluxes are tabulated at column 12.

References. (A1) Carollo et al. (2002) (A2) Quillen et al. (2001); (A3) Galliano & Alloin (2008); (A4) Simpson (1998); (A5) Meisenheimer et al. (2007); (A6) Peng et al. (2006); (A7) Alonso-Herrero et al. (2011); (B1) Ramos Almeida et al. (2009); (B2) This work.

sources are MCG-5-23-16, NGC 2110, and NGC 7582 (Alonso-Herrero et al. 2011). All the references used for dividing the sample into each subgroup are indicated in column 12 in Table 1.

Finally, the sources in this study are categorized into three groups (type-1, HBLR, and NHBLR; see column 6 in Table 1). The sample contains 4 type-1, 10 HBLR, and 7 NHBLR AGN.

3. APPLICATION OF TORUS MODEL

3.1. Clumpy Torus Model

We fit the clumpy torus models of Nenkova et al. (2008a), known as *CLUMPY*, to the data using a Bayesian approach (BAYESCLUMPY; Asensio Ramos & Ramos Almeida 2009). Here we describe the six free *CLUMPY* model parameters used for the SED fitting and the model set-up, which are listed in Table 3. The torus clumps are distributed in a smooth, rather than sharp, toroidal-shaped boundary of angular width σ . The inner radius (r_{in}) of the torus is set by the location of the dust at the sublimation temperature ($T_{\text{sub}} \sim 1500$ K). This is computed using the AGN bolometric luminosity $L_{\text{bol}}(\text{AGN})$

$$r_{\text{in}} = 0.4 \left(\frac{L_{\text{bol}}(\text{AGN})}{10^{45} \text{ erg s}^{-1}} \right)^{0.5} \text{ pc.} \quad (1)$$

The torus has a radial extent (Y) defined by $Y = r_{\text{out}}/r_{\text{in}}$, where r_{out} is the outer radius of the torus. The average number of clouds along the line of sight (N_{LOS})

at a viewing angle i is set as

$$N_{\text{LOS}} = N_0 \exp \left[-\frac{(90 - i)^2}{\sigma^2} \right], \quad (2)$$

where N_0 is the average number of clouds along the radial equatorial ray. N_{LOS} allows us to derive the escape probability of photons from the AGN central engines (P_{esc}). In the *CLUMPY* dust distribution, the classification of type-1 or type-2 AGN depends on whether or not there is a clump along the line of sight, which is a function of the viewing angle of the torus, the number of clumps and the torus width. This is different from smooth torus models, for which the classification of an AGN as type-1 or type-2 is solely determined by the viewing angle. The escape probability of photons passing through the torus at a given viewing angle (i) can be calculated as

$$P_{\text{esc}} \sim e^{-N_{\text{LOS}}}. \quad (3)$$

In the *CLUMPY* model, the radiative transfer equations are solved for each clump and thus the calculations depend on the clump distribution within the torus, the optical depth of each clump, and also its dust composition. Here we assume each clump has the same optical depth (τ_V), which is defined at the optical V band. The *CLUMPY* model applies a standard cold oxygen-rich interstellar medium dust, which is called OHMc dust (Ossenkopf et al. 1992). The torus clumps are distributed as a power law with index q as a function of radius, $N(r) \propto r^{-q}$.

In addition to these six physical parameters, we add

TABLE 3
FREE PARAMETERS OF THE BAYESCLUMPY

Parameters	Parameter range
Torus radial thickness (Y)	[5, 30]
Torus angular width (σ)	[15°, 70°]
Number of clouds along an equatorial ray (N_0)	[1, 15]
Index of the radial density profile (q)	[0, 3]
Viewing angle (i)	[0°, 90°]
Optical depth of each cloud (τ_V)	[5, 150]

NOTE. — Torus radial thickness Y is defined as $Y = r_{\text{out}}/r_{\text{in}}$, where r_{out} is the outer radius and r_{in} is the inner radius. The cloud distribution between r_{out} and r_{in} is parameterized as r^{-q} .

two additional parameters to be fitted or fixed. The first parameter is the foreground extinction (A_V), unrelated to the torus. Some authors demonstrated that some AGN have an extremely deep 9.7 μm silicate absorption feature which cannot be reproduced solely by the torus obscuration (Alonso-Herrero et al. 2003; Polletta et al. 2008; Alonso-Herrero et al. 2011; Goulding et al. 2012; González-Martín et al. 2013). They suggested that dust in inclined host galaxies can contribute significantly to the observed SED and silicate feature absorption. 10 out of 21 sources are inclined galaxies with low minor-to-major axis ratios ($b/a \leq 0.5$; see Table 1). Therefore, some portion of the observed SED is accounted for by cool foreground dust extinction. Alonso-Herrero et al. (2011) discussed this issue and concluded that for $A_V \geq 5$, the effects of foreground extinction cannot be ignored for reproducing the silicate 9.7 μm feature. We gathered available values of foreground A_V from the literature and compiled them in column 10 in Table 1. The other additional parameter accounts for the multiplicative factor that has to be applied to match the fluxes of a given model to an observed SED. Deriving this factor enables us to calculate the model AGN bolometric luminosity $L_{\text{bol}}^{(\text{mod})}$ (Nenkova et al. 2008b). As shown by Alonso-Herrero et al. (2011), $L_{\text{bol}}^{(\text{mod})}$ reproduces well the values of $L_{\text{bol}}^{(\text{lit})}$ for Seyfert galaxies, and therefore, in the following we will refer to $L_{\text{bol}}^{(\text{mod})}$ as the bolometric luminosities of the sample studied here.

By combining the derived output parameters of the *CLUMPY* model, we can derive other important torus morphological parameters as the torus outer radius r_{out} , defined as:

$$r_{\text{out}} = r_{\text{in}} Y \text{ pc.} \quad (4)$$

We can also calculate the torus scale height H as:

$$H = r_{\text{out}} \sin \sigma \text{ pc.} \quad (5)$$

Finally, we define the “geometrical” torus covering factor, which is unaffected by the viewing angle, and it is defined by integrating the AGN escape probability over all angles (Nenkova et al. 2008a). This can be written as

$$C_T = 1 - \int_0^{\pi/2} P_{\text{esc}}(\beta) \cos(\beta) d\beta, \quad (6)$$

where $\beta = \pi/2 - i$. Considering that our motivation is to characterize the intrinsic torus morphology, the “geometrical” torus covering factor is more relevant here than the apparent covering factor.

3.2. BAYESCLUMPY and Modeling Details

The *CLUMPY* database currently contains more than 5×10^6 models. Therefore, when fitting the models to the observations, inherent degeneracies have to be taken into account. We then use the BAYESCLUMPY fitting tool (Asensio Ramos & Ramos Almeida 2009), as it does a fast synthesis of the *CLUMPY* SEDs. In the last version of BAYESCLUMPY the inference over the model parameters can be done either using neural network interpolation or multilinear interpolation in the full database. After running several tests, Ramos Almeida et al. (2014) concluded that the latter interpolation produces more robust results. Therefore, here we use linear interpolation, which results in slight differences in the fitted parameters (within 1σ for the majority of the fits) for the 13 galaxies that were modeled by Alonso-Herrero et al. (2011) using the neural network interpolation and subsequently re-fitted in this paper.

BAYESCLUMPY can be used to fit photometry and/or spectra in a Bayesian scheme, carrying out inference over the model parameters for observed SEDs. This way we can specify a-priori information about the model parameters. Here we consider uniform prior distribution in the range of each parameter, as summarized in Table 3. The prior distribution of inclination angle (i) is fixed from previous observations if available in the literature, following the same approach as in Alonso-Herrero et al. (2011). From the objects in our sample taken from González-Martín et al. (2013), NGC 1386 has two possible inclination angles 65° and 85° (Levenson et al. 2006). Thus, we use a uniform prior in the range 60°–90° for this source. For the galaxies taken from Alonso-Herrero et al. (2011), we use the same inclination angle constraints they employed, which are compiled in column 11 in Table 1.

We finally include the AGN direct emission (i.e. a broken power-law) which is defined in Eq. (13) of Nenkova et al. (2008a) to the SED for type-1 AGN, in order to reproduce the flatter slope of the NIR band (see Ramos Almeida et al. 2014, for further details).

4. RESULTS AND DISCUSSIONS

4.1. Infrared SEDs with BAYESCLUMPY Fitting

The results of the fitting process to the IR SEDs are the posterior distributions for the six parameters that describe the model (defined in Table 3), the foreground extinction and the multiplicative factor needed to match the SED fluxes. However, we can also translate the results into corresponding spectra, as shown in Figure 1.

Figure 1 shows the observed SEDs and nuclear MIR spectra (black filled dots) of the galaxies with the best fit results overlaid (blue solid lines), based on the inference done with BAYESCLUMPY. The fitted models correspond to those described by the median of the posterior distribution of each parameter. All the derived torus parameters obtained from BAYESCLUMPY are presented in Table 4.

Some SEDs show lower Q -band fluxes than those predicted by the fitted model. This effect is prominent when silicate 9.7 μm feature is observed in deep absorption. Although this may suggest that the model spectra still have a difficulty to reproduce the 18 μm silicate feature, the difference is only within a factor of 3 in the worst case (NGC 3281). See Ramos Almeida et al. (2009) for

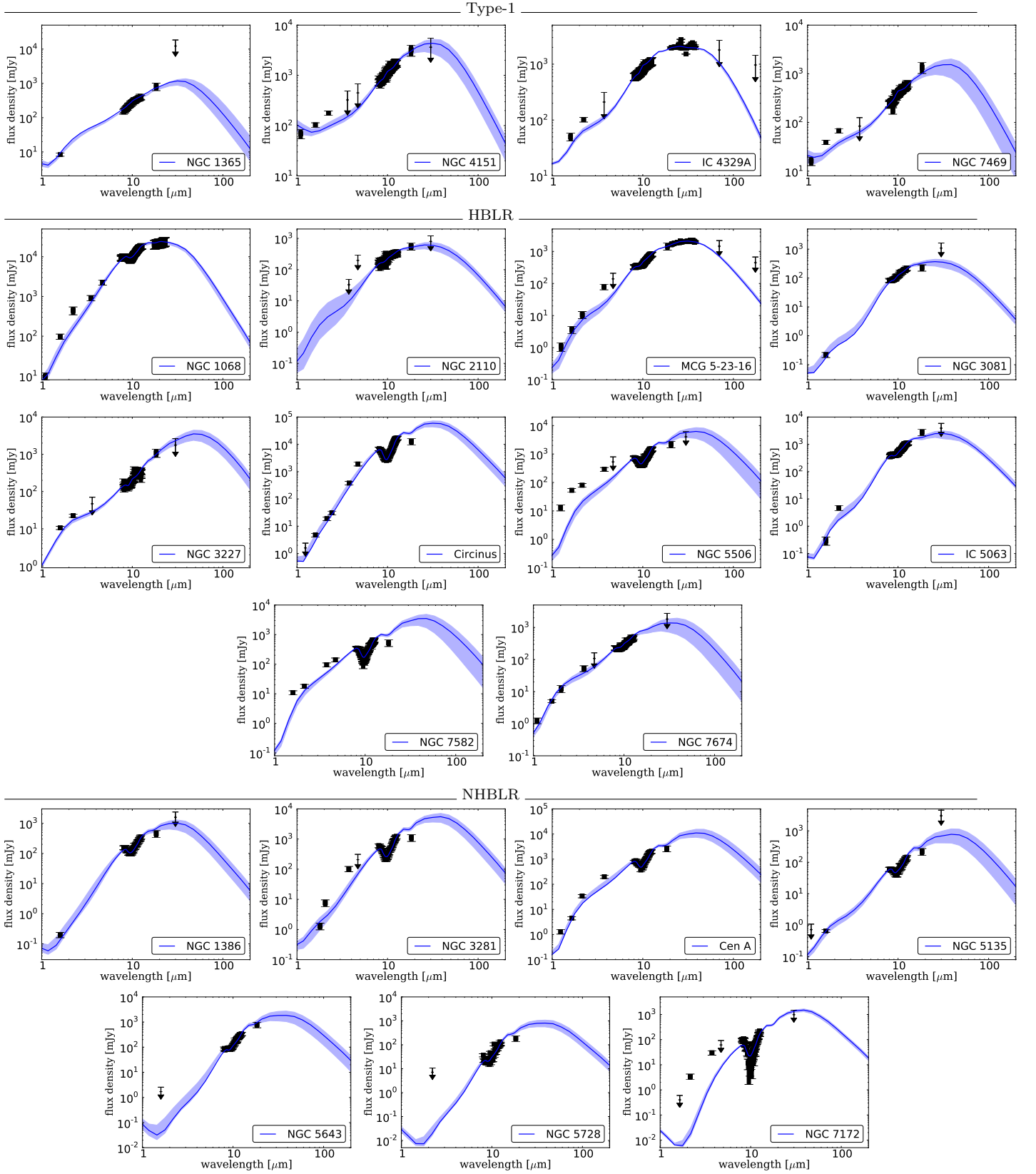


FIG. 1.— Clumpy torus model fits. The filled dots are the photometric data and the black line is the MIR spectrum. The upper limit points are shown as arrows. The solid blue lines are the models computed with the median value of the probability distribution of each parameter. The blue shaded areas indicate the range of models compatible with a 68% confidence interval. For the details on the calculation of the median values, see Section 3.

TABLE 4
FITTED TORUS MODEL PARAMETERS FROM SED + SPECTROSCOPY DATA

Galaxy	σ_{torus} [deg]	Y	N_0	q	τ_V	i [deg]	C_T	$\log L_{\text{bol}}^{(\text{mod})}$ [erg/s]	r_{in} [pc]	r_{out} [pc]	H [pc]
Type-1											
NGC 1365	19^{+5}_{-2}	24^{+3}_{-4}	9^{+2}_{-3}	$0.3^{+0.3}_{-0.4}$	79^{+42}_{-35}	19^{+19}_{-11}	$0.16^{+0.08}_{-0.04}$	$43.2^{+0.8}_{-0.1}$	$0.053^{+0.005}_{-0.005}$	$1.3^{+0.2}_{-0.3}$	$0.4^{+0.1}_{-0.1}$
NGC 4151	16^{+1}_{-1}	19^{+4}_{-4}	13^{+1}_{-1}	$1.6^{+0.3}_{-0.3}$	89^{+8}_{-8}	71^{+2}_{-2}	$0.13^{+0.03}_{-0.02}$	$43.9^{+0.9}_{-0.1}$	$0.108^{+0.007}_{-0.008}$	$2.1^{+0.5}_{-0.5}$	$0.6^{+0.2}_{-0.1}$
IC 4329A	40^{+1}_{-1}	8^{+1}_{-1}	12^{+1}_{-1}	$0.5^{+0.1}_{-0.1}$	148^{+1}_{-2}	4^{+4}_{-3}	$0.58^{+0.04}_{-0.04}$	$44.4^{+1.8}_{-0.1}$	$0.192^{+0.002}_{-0.001}$	$1.8^{+0.1}_{-0.1}$	$1.1^{+0.0}_{-0.0}$
NGC 7469	21^{+2}_{-2}	22^{+4}_{-4}	13^{+1}_{-1}	$1.3^{+0.3}_{-0.3}$	124^{+12}_{-14}	59^{+3}_{-4}	$0.20^{+0.05}_{-0.04}$	$44.6^{+0.8}_{-0.1}$	$0.239^{+0.020}_{-0.021}$	$5.3^{+1.1}_{-1.2}$	$1.9^{+0.4}_{-0.4}$
HBLR											
NGC 1068	56^{+8}_{-18}	6^{+2}_{-1}	5^{+3}_{-1}	$0.6^{+1.2}_{-0.4}$	38^{+3}_{-7}	67^{+11}_{-5}	$0.78^{+0.06}_{-0.19}$	$44.4^{+0.9}_{-0.1}$	$0.198^{+0.015}_{-0.006}$	$1.3^{+0.6}_{-0.1}$	$1.1^{+0.3}_{-0.1}$
NGC 2110	55^{+8}_{-8}	17^{+7}_{-6}	9^{+2}_{-2}	$2.7^{+0.2}_{-0.3}$	146^{+2}_{-4}	40^{+5}_{-6}	$0.88^{+0.05}_{-0.11}$	$43.3^{+1.0}_{-0.1}$	$0.058^{+0.003}_{-0.002}$	$1.0^{+0.5}_{-0.4}$	$0.8^{+0.4}_{-0.4}$
MCG -5-23-16	58^{+5}_{-8}	20^{+2}_{-1}	7^{+2}_{-1}	$2.1^{+0.2}_{-0.1}$	144^{+3}_{-6}	48^{+7}_{-3}	$0.85^{+0.03}_{-0.05}$	$43.9^{+1.2}_{-0.1}$	$0.114^{+0.004}_{-0.003}$	$2.3^{+0.3}_{-0.2}$	$2.0^{+0.3}_{-0.3}$
NGC 3081	62^{+4}_{-5}	11^{+9}_{-4}	12^{+1}_{-1}	$2.6^{+0.2}_{-0.4}$	98^{+12}_{-11}	66^{+13}_{-19}	$0.96^{+0.02}_{-0.03}$	$43.1^{+1.0}_{-0.1}$	$0.043^{+0.003}_{-0.003}$	$0.4^{+0.5}_{-0.1}$	$0.3^{+0.4}_{-0.1}$
NGC 3227	57^{+1}_{-1}	20^{+1}_{-1}	13^{+1}_{-1}	$0.0^{+0.1}_{-0.0}$	147^{+1}_{-2}	6^{+5}_{-4}	$0.94^{+0.01}_{-0.02}$	$43.0^{+1.0}_{-0.1}$	$0.041^{+0.003}_{-0.003}$	$0.8^{+0.1}_{-0.1}$	$0.7^{+0.1}_{-0.1}$
Circinus	64^{+3}_{-5}	16^{+2}_{-1}	12^{+1}_{-2}	$0.4^{+0.3}_{-0.2}$	35^{+2}_{-2}	37^{+8}_{-7}	$0.96^{+0.02}_{-0.03}$	$43.4^{+1.0}_{-0.1}$	$0.062^{+0.004}_{-0.003}$	$1.0^{+0.2}_{-0.2}$	$0.9^{+0.2}_{-0.1}$
NGC 5506	48^{+6}_{-6}	16^{+3}_{-2}	10^{+2}_{-3}	$0.2^{+0.3}_{-0.2}$	79^{+4}_{-5}	32^{+4}_{-1}	$0.79^{+0.04}_{-0.05}$	$44.0^{+1.0}_{-0.1}$	$0.130^{+0.008}_{-0.007}$	$2.1^{+0.5}_{-0.5}$	$1.6^{+0.4}_{-0.3}$
IC 5063	61^{+4}_{-6}	14^{+7}_{-7}	12^{+1}_{-1}	$2.5^{+0.2}_{-1.1}$	101^{+7}_{-9}	77^{+7}_{-12}	$0.96^{+0.02}_{-0.04}$	$44.3^{+1.0}_{-0.1}$	$0.182^{+0.009}_{-0.008}$	$2.6^{+1.6}_{-1.4}$	$2.3^{+1.4}_{-1.3}$
NGC 7582	53^{+3}_{-2}	20^{+2}_{-6}	12^{+1}_{-2}	$0.1^{+0.1}_{-0.0}$	79^{+7}_{-9}	6^{+5}_{-4}	$0.90^{+0.02}_{-0.02}$	$43.5^{+0.9}_{-0.1}$	$0.070^{+0.005}_{-0.004}$	$1.4^{+0.3}_{-0.2}$	$1.2^{+0.2}_{-0.2}$
NGC 7674	39^{+13}_{-9}	15^{+5}_{-4}	8^{+3}_{-3}	$1.1^{+0.5}_{-0.6}$	133^{+9}_{-15}	44^{+13}_{-13}	$0.56^{+0.17}_{-0.20}$	$44.8^{+0.5}_{-0.1}$	$0.330^{+0.020}_{-0.038}$	$5.3^{+2.5}_{-1.7}$	$3.3^{+1.4}_{-1.0}$
NHBLR											
NGC 1386	56^{+7}_{-9}	19^{+5}_{-5}	8^{+2}_{-1}	$1.3^{+0.3}_{-0.2}$	37^{+4}_{-4}	68^{+9}_{-5}	$0.87^{+0.05}_{-0.11}$	$42.5^{+0.8}_{-0.1}$	$0.023^{+0.002}_{-0.002}$	$0.5^{+0.1}_{-0.1}$	$0.4^{+0.1}_{-0.1}$
NGC 3281	68^{+1}_{-2}	19^{+3}_{-2}	14^{+1}_{-1}	$0.4^{+0.2}_{-0.2}$	38^{+3}_{-4}	19^{+6}_{-6}	$0.99^{+0.01}_{-0.01}$	$44.2^{+0.9}_{-0.1}$	$0.151^{+0.010}_{-0.008}$	$2.9^{+0.6}_{-0.4}$	$2.7^{+0.5}_{-0.4}$
Cen A	50^{+10}_{-9}	17^{+3}_{-3}	10^{+2}_{-2}	$0.3^{+0.3}_{-0.2}$	89^{+11}_{-13}	38^{+8}_{-9}	$0.81^{+0.10}_{-0.16}$	$42.5^{+0.8}_{-0.1}$	$0.021^{+0.002}_{-0.002}$	$0.4^{+0.1}_{-0.1}$	$0.3^{+0.1}_{-0.1}$
NGC 5135	63^{+3}_{-5}	17^{+5}_{-2}	12^{+1}_{-2}	$0.4^{+0.4}_{-0.3}$	71^{+5}_{-6}	17^{+10}_{-10}	$0.97^{+0.01}_{-0.04}$	$43.6^{+0.8}_{-0.1}$	$0.079^{+0.007}_{-0.006}$	$1.4^{+0.4}_{-0.3}$	$1.2^{+0.4}_{-0.3}$
NGC 5643	62^{+4}_{-6}	14^{+4}_{-2}	13^{+1}_{-1}	$0.8^{+0.5}_{-0.5}$	56^{+11}_{-9}	74^{+8}_{-12}	$0.97^{+0.02}_{-0.04}$	$43.0^{+0.8}_{-0.1}$	$0.040^{+0.004}_{-0.003}$	$0.6^{+0.2}_{-0.1}$	$0.5^{+0.2}_{-0.1}$
NGC 5728	66^{+2}_{-3}	17^{+2}_{-1}	14^{+1}_{-1}	$0.7^{+0.4}_{-0.4}$	48^{+7}_{-6}	80^{+5}_{-8}	$0.99^{+0.01}_{-0.01}$	$43.4^{+0.9}_{-0.1}$	$0.063^{+0.004}_{-0.004}$	$1.1^{+0.2}_{-0.1}$	$1.0^{+0.1}_{-0.1}$
NGC 7172	69^{+1}_{-1}	29^{+1}_{-1}	14^{+1}_{-1}	$0.0^{+0.1}_{-0.0}$	20^{+1}_{-1}	50^{+3}_{-3}	$0.99^{+0.01}_{-0.01}$	$43.4^{+1.2}_{-0.1}$	$0.064^{+0.002}_{-0.002}$	$1.9^{+0.1}_{-0.1}$	$1.8^{+0.1}_{-0.1}$

Notes.— Torus model parameters derived from the fits with BAYESCLUMPY. Median values of each posterior distribution are listed with their corresponding $\pm 1\sigma$ values around the median.

TABLE 5
TORUS MODEL PARAMETERS FROM THE GLOBAL POSTERIOR DISTRIBUTIONS

AGN Type	σ_{torus} [deg]	Y	N_0	q	τ_V	i [deg]	C_T	$\log L_{\text{bol}}^{(\text{mod})}$ [erg/s]	r_{in} [pc]	r_{out} [pc]	H [pc]
All	56^{+6}_{-22}	18^{+2}_{-6}	12^{+1}_{-4}	$0.5^{+0.6}_{-0.5}$	81^{+23}_{-43}	45^{+14}_{-31}	$0.88^{+0.06}_{-0.38}$	$43.3^{+0.5}_{-0.4}$	$0.066^{+0.048}_{-0.030}$	$1.2^{+0.4}_{-0.8}$	$1.0^{+0.3}_{-0.6}$
Type-1	19^{+3}_{-3}	19^{+3}_{-10}	12^{+0}_{-2}	$0.7^{+0.5}_{-0.5}$	113^{+20}_{-31}	52^{+9}_{-48}	$0.18^{+0.06}_{-0.06}$	$43.9^{+0.3}_{-0.8}$	$0.144^{+0.048}_{-0.090}$	$1.6^{+0.4}_{-0.4}$	$1.0^{+0.0}_{-0.6}$
HBLR	56^{+4}_{-8}	17^{+2}_{-8}	11^{+1}_{-4}	$0.8^{+1.2}_{-0.8}$	98^{+34}_{-60}	43^{+9}_{-32}	$0.88^{+0.04}_{-0.14}$	$43.7^{+0.2}_{-0.7}$	$0.066^{+0.054}_{-0.024}$	$1.2^{+0.8}_{-0.4}$	$1.0^{+0.6}_{-0.3}$
NHBLR	64^{+2}_{-11}	18^{+3}_{-3}	13^{+0}_{-3}	$0.4^{+0.2}_{-0.4}$	43^{+17}_{-11}	48^{+17}_{-28}	$0.96^{+0.02}_{-0.10}$	$43.2^{+0.1}_{-0.8}$	$0.060^{+0.006}_{-0.042}$	$0.8^{+0.8}_{-0.4}$	$1.0^{+0.3}_{-0.6}$

Notes.— Torus parameters from the global posterior distributions of each subgroup.

further discussion on the Q -band excess.

The SEDs of NGC 5506 and NGC 7172 show NIR excesses compared to the model spectra as shown in Figure 1. NIR interferometric observations (Kishimoto et al. 2009, 2011) and NIR reverberation mapping (Kishimoto et al. 2007; Koshida et al. 2009) of Seyfert galaxies suggest that the AGN torus has much smaller sublimation radius than expected from Eq. (1). Kawaguchi & Mori (2011) also showed in their model that if they add the rim darkening effect of the accretion disk, the torus inner radius naturally connects to the outer disk. Thus, the NIR excess is readily accounted for by this connection. This is also shown in Stalevski et al. (2012) when they apply the rim darkening effect to produce the model SEDs. However, in this study, we did not include the SED of a hot dust component or apply such torus geometry including rim darkening effect for the fitting as this hot dust remains rather unconstrained. Further discussion on the possible origins of NIR excesses can be found in Alonso-Herrero et al. (2011).

4.2. General Torus Properties for Whole Sample

In this section, we describe how we obtained the global distribution of the torus model parameters for the whole sample and the three subgroups considered here. To take full advantage of the data employed here, we apply a hierarchical Bayesian approach to derive information about the global distribution of the *CLUMPY* parameters for a given subgroup. We use a generalized beta distribution as the prior for each parameter (given that they are defined in closed intervals) and learn the hyperparameters of the prior using importance sampling (e.g. Brewer & Elliott 2014). This allows us to derive the posterior distribution for each parameter taking into account all the observed data that belongs to an AGN subgroup.

In Table 5 we report the median parameters of the global posterior distributions for the whole sample, as well as for each subgroup. Note that the global posterior distribution of each parameter can be derived only in the circumstance that the prior distribution is the same for all the sources. This is not the case for the inclination angle because we use the constrained prior distributions for some sources as described in Section 3. For the inclination angle, we derive the median parameters of the individual galaxy fits within the each subgroup.

Based on interferometric observations, Kishimoto et al. (2011) reported a typical torus half-light radius of ~ 1 pc for local AGN at MIR wavelengths. Our derived torus outer radius $r_{\text{out}} = 1.2_{-0.8}^{+0.4}$ pc is consistent with the interferometry results, although a little larger. This is understood because here we are considering colder dust within the torus than that traced by the MIR interferometry, as we include data at $\lambda > 20 \mu\text{m}$ in our fits. These colder clumps will be generally located at larger radii, which explain the value of r_{out} obtained from the global posterior distribution. The torus outer radius including cooler dust would be larger still than the value of $r_{\text{out}} \sim 1.2$ pc. Further studies including *Herschel*, SOFIA, and/or ALMA observations will help constraining the extent of the FIR-emitting dust. Indeed, some pilot studies already showed the importance of FIR data to trace cooler dust (Ramos Almeida et al. 2011b; García-Burillo et al. 2014).

4.3. Distribution of Torus Model Parameters

The key science direction of this paper is to investigate the torus morphology quantitatively by deriving torus parameters for each subgroup and comparing them. The median values of the model parameters fitted to our nuclear IR SEDs are reported in Table 4. The median values of the global posterior distributions of the free parameters σ , Y , N_0 , q , and τ_V for each subgroup are compiled in Table 5. As discussed in Section 4.2, for the inclination angle i we derive the median values from the individual galaxy fits for each subgroup.

Figure 2 shows the global posterior distributions of each physical parameter for the different subgroups. Black, blue, red, and green histograms show the parameter distribution of all, type-1, HBLR, and NHBLR sources, respectively.

As shown in Figure 2, for some of the parameters, the global distributions are similar for the three subgroups, but others are clearly different. In order to quantify these differences, we follow the same approach as in Ramos Almeida et al. (2011a). They used the Kullback-Leibler divergence (KLD; Kullback & Leibler 1951) to show that the joint posterior distributions of type-1 and type-2 AGN were quantitatively different. The KLD takes into account the full shape of two posterior distributions to compare them. When the two distributions are identical, the value is $\text{KLD} = 0$ and, the larger the KLD value, the more different the two distributions. Ramos Almeida et al. (2011a) concluded that if $\text{KLD} > 1.0$, the two posteriors can be considered significantly different. We calculate the KLD values for the global distributions of each torus parameter among the three groups. The values are reported in Table 6.

We find significant differences for the parameters σ , Y , and N_0 between type-1 AGN and HBLR AGN. The differences in these parameters between type-1 and type-2 AGN were already reported in Ramos Almeida et al. (2011a) with larger significance, but based on fits to NIR and MIR photometry only, where spectroscopic data were not included. Besides, they did not consider information from spectropolarimetry data, as we are doing here. Therefore, we confirm the results of Ramos Almeida et al. (2011a) after including N band spectroscopy to the IR photometry, which is crucial to constrain the six torus parameters (Alonso-Herrero et al. 2011; Ramos Almeida et al. 2014). We also find that the parameters σ , Y , and N_0 of HBLR and NHBLR AGN are significantly different. Considering the average values in Table 5, the tori of NHBLR AGN have larger σ , larger Y , and larger N_0 than those of HBLR AGN.

There are various possible interpretations for the difference in σ among the subgroups. One possibility is that the smaller σ could be due to larger AGN luminosities (receding torus model; Lawrence 1991; Ricci et al. 2013). However, as shown in Table 5, the differences of median bolometric AGN luminosities among the subgroups are within the uncertainties. Therefore, we consider that the effect of the AGN luminosity is negligible in this study. Another possible interpretation is a selection bias in the optical type-1/type-2 AGN selection. Ramos Almeida et al. (2011a) and Elitzur (2012) discussed that AGN classification would depend on the distribution of the obscuring material; type-1 AGN would be preferen-

TABLE 6
 RESULTS OF KLD TEST FOR EACH PARAMETER AMONG EACH SUBGROUP

AGN Type	σ_{torus}	Y	N_0	q	τ_V
Type-1 vs HBLR	3.13	1.26	0.10	0.42	0.10
Type-1 vs NHBLR	2.22	0.22	0.05	0.20	4.83
HBLR vs NHBLR	1.78	1.63	0.24	0.53	1.56

Notes.— KLD is calculated for the global posterior distribution of each parameter among the subgroups. Values larger than 1 are shown in bold.

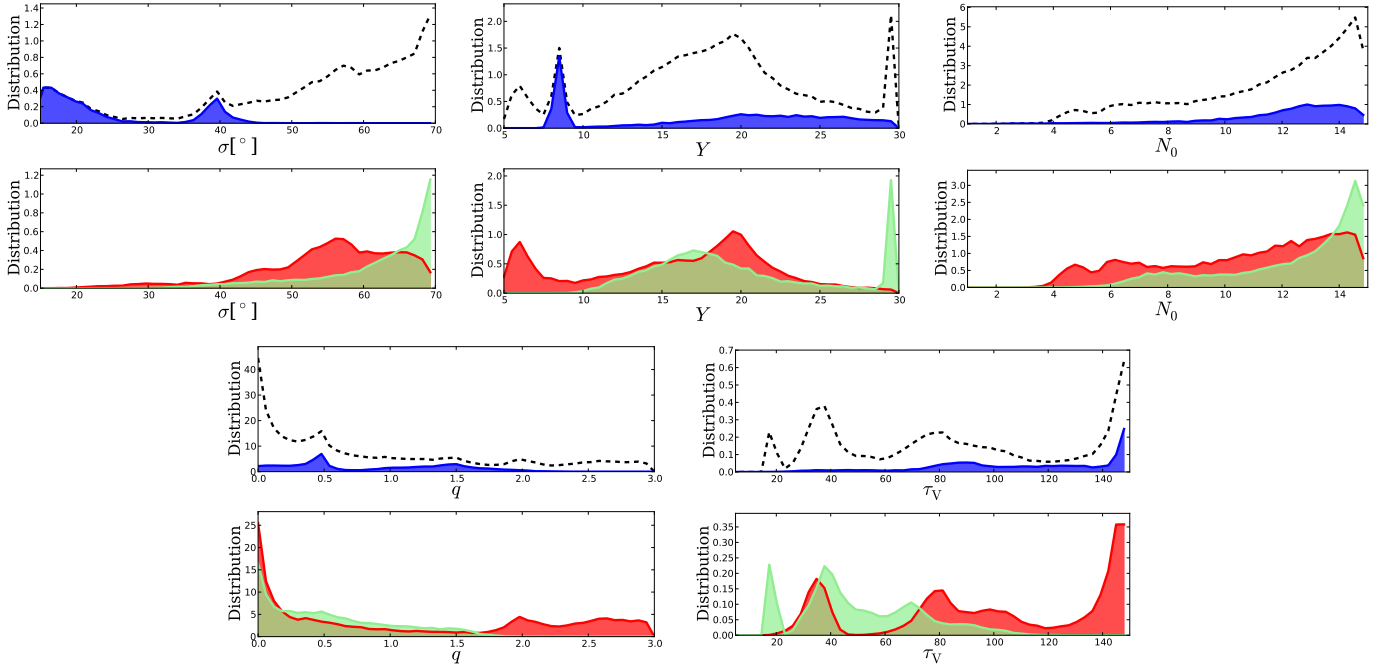


FIG. 2.— Histograms of each physical parameter discussed in Section 4.3. Top panel of each figure represents the histogram of the whole sample. Blue/red/green filled color represents the histogram of Type-1/HBLR/NHBLR, respectively.

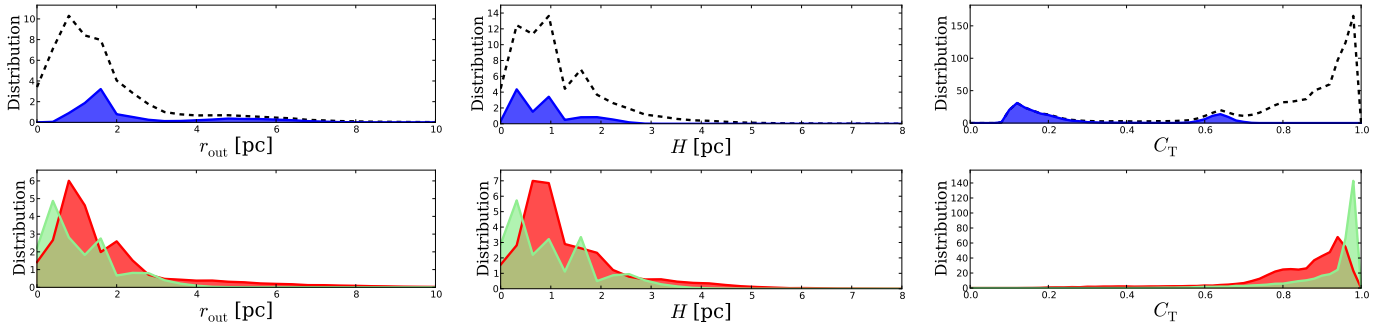


FIG. 3.— Same as in Figure 1, but for the r_{out} , H , and C_T parameters.

tially selected from lower-obscuration AGN, while type-2 AGN (HBLR and NHBLR) from higher-obscuration AGN. This could be partly producing the differences in σ that we found for type-1 and type-2 AGN, but correcting this effect quantitatively is extremely difficult and beyond the scope of this paper.

4.4. Distribution of Covering Factor

As shown in Section 3.1., we can derive physical parameters of the torus model by combining the model pa-

rameters. The individual values of these physical parameters are reported in Table 4, and those obtained from the global posterior distribution for each subgroup are shown in Figure 3 and Table 5.

An interesting comparison can be made between the geometrical covering factor of the torus model (C_T ; described in equation 6) of the different subgroups and the average column densities derived from X-ray data (N_H). NHBLRs have the largest column densities, with an average value of $\log N_H \sim 24.0 \text{ cm}^{-2}$ (i.e. Compton-

thick), followed by HBLRs, with $\log N_{\text{H}} \sim 23.4 \text{ cm}^{-2}$, and type-1s, with $\log N_{\text{H}} \sim 21.8 \text{ cm}^{-2}$. Based on hard X-ray (50–200 keV) observations of nearby AGN obtained with *INTEGRAL*, Ricci et al. (2011) reported differences between the X-ray reflection component of type-1 and type-2 AGN. Type-1 and “lightly obscured” AGN with $N_{\text{H}} \leq 10^{23} \text{ cm}^{-2}$ have the same X-ray reflection component, with reflection amplitude $R \sim 0.4$. On the other hand, “mildly obscured” AGN ($N_{\text{H}} \geq 10^{23} \text{ cm}^{-2}$) show a clearly stronger X-ray reflection component with $R \sim 2.2$, suggesting that the central engine of “mildly obscured” AGN would be covered by an X-ray reflection wall. Our results are in good agreement with Ricci et al. (2011) if we consider the C_{T} and N_{H} values for each subgroup. The type-1 AGN in our sample fall in the “lightly obscured” AGN in their study, and indeed they show small covering factors ($C_{\text{T}} \sim 0.18$), suggesting small torus X-ray reflection solid angle. The HBLR and NHBLR AGN subgroups would fall in the “mildly obscured” AGN category, and we found large covering factors for them ($C_{\text{T}} \sim 0.88$ and 0.96 respectively), suggesting a larger X-ray reflection component (see also Ricci et al. 2014). Figure 4 shows a schematic illustration of the torus geometrical differences among type-1 (top), HBLR (middle), and NHBLR (bottom).

4.5. Torus Model Morphological Differences between HBLR and NHBLR

In this section we focus on the differences between the modeled tori of HBLR and NHBLR. In the case of HBLR, we obtain smaller σ values than for NHBLR, which is equivalent to larger torus opening angles ($90^\circ - \sigma$). This implies that HBLR objects can have a larger scattering region. (see middle panel of Figure 4). The scattering region (shown schematically as a filled green bar) can be larger due to the larger opening angle of the torus, allowing more photons to be scattered, and hence polarized, from the BLR. We note that the larger opening of the ionization cone, if unresolved, will produce a slightly lower degree of polarization due to (partial) cancellation of those polarization vectors at the edges of the scattering region. However, in our case, the increased amount of scattered photons will significantly increase the polarized flux, with only a very small reduction in the degree of polarization. To confirm this effect, we produced a toy polarization model assuming that the scattering region is a two dimensional biconical structure centered to the central engine. Then, we measure the degree of polarization and polarized flux, and found that the measured polarized flux is larger for HBLR than those for NHBLR, supporting our results. Miller & Goodrich (1990) also find the same results using a 3 dimensional cone and more sophisticated modeling, and more complex assumptions.

In the case of the NHBLR, we obtain larger σ values than for HBLR. This means that the probability that scattered radiation from the BLR can be blocked is higher than for HBLR objects. This is also in agreement with the larger value of $\log N_{\text{H}} \sim 24.0 \text{ cm}^{-2}$ estimated from X-ray observations of the NHBLR objects in our sample.

To summarize, as shown in the bottom panel of Figure 4, the chance to observe scattered (polarized) flux from the BLR is reduced by the double effect of (a) less scattering of the flux from the BLR (due to the reduced

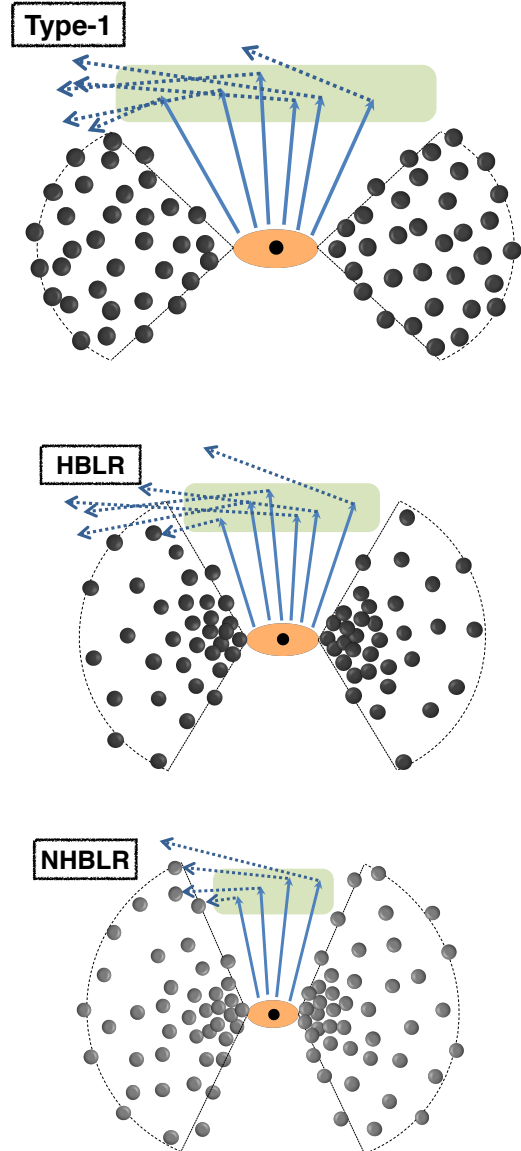


FIG. 4.— Schematic illustration of the torus geometry for type-1 AGN (top), HBLR (middle), and NHBLR (bottom). The difference in color intensity between the two bottom panels shows the difference in optical depth of the clumps τ_{ν} , where darker color is larger τ_{ν} . The orange region represents the BLR. The green area represents the media where some of the incoming BLR emission is scattered and then polarized (in all diagrams we describe only scattering from the polar scattering region, and ignore the inner equatorial scattering region, dominantly responsible for the polarized flux in Type 1 objects). The blue solid arrows represent the path of BLR photons and the blue dashed arrows represent the path of the polarized BLR photons. The observer is assumed to be on the left side of the torus with an inclination angle of 52° , 43° , and 48° , respectively (see Table 5). The only photons scattered along these lines of sight are shown.

scattering area) and (b) more obscuration between the observer and the scattering region. Therefore, the classification of an AGN as HBLR or NHBLR is probabilistic, and it would depend on the intrinsic properties of the torus, in particular of σ . This could be a reasonable ex-

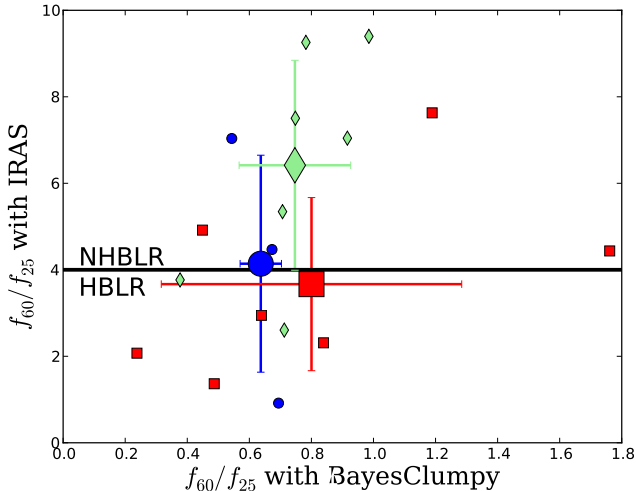


FIG. 5.— Plot comparing the f_{60}/f_{25} colors measured from *IRAS* photometry and extrapolated from the clumpy torus model fits. Blue circle/red square/green diamond represents type-1, HBLR, and NHBLR AGN, respectively. The larger symbol represents the average value of each subgroup. The horizontal line at $f_{60}/f_{25} = 4$ is the boundary between HBLR and NHBLR AGN according to Heisler et al. (1997), where HBLR AGN have $f_{60}/f_{25} < 4$ and NHBLR AGN $f_{60}/f_{25} > 4$.

planation for the lack of a hidden (polarized) BLR in some type-2 objects⁴.

However, we note that the classification of the galaxies as HBLR and NHBLR is mainly based on spectropolarimetric observations from 3–4 m telescopes, and some of the NHBLR could be then misclassified. Therefore, further higher sensitivity spectropolarimetry observations of NHBLR AGN with 8 m class telescopes such as Subaru/FOCAS and/or VLT/FORS2 are highly encouraged to search for the HBLR in those AGN (Ramos Almeida et al. in prep.).

4.6. Inclination Angle Effect on Detectability of HBLR in Type-2 AGN

The dependence of HBLR detection in type-2 AGN on torus inclination angle is still a matter of debate. This idea arises from the observational trend that the *IRAS* 60 μm to 25 μm color ratio (f_{60}/f_{25}) of HBLR AGN is $f_{60}/f_{25} < 4$ on average while that of NHBLR AGN is $f_{60}/f_{25} > 4$ (Heisler et al. 1997; Lumsden et al. 2001). Several authors have suggested that this trend is due to the inclination angle of the torus: the cooler and outer dust within the torus blocks the warm and inner hot dust for edge-on views, producing the high f_{60}/f_{25} , while the warm inner dust can be seen from the face-on views, reducing the value of f_{60}/f_{25} . Following this idea, type-2 AGN with low f_{60}/f_{25} would tend to be detected as HBLR AGN due to the more face-on view of the torus and vice versa.

Here we can take advantage of the torus models fitted to our SEDs, which are available for each AGN and

⁴ A similar explanation for the lack of HBLR detection in $\sim 40\%$ of type-2 objects, based on the distribution of dust within the torus and its inclination being not as simple as predicted by the unified model, was shown in the talk by C. Ramos Almeida at the Polarization & active galactic nuclei workshop held 2012 October 16–17 at the Royal Observatory of Belgium.

shown in Figure 1. The wavelength range covered by the models allows us to calculate f_{60}/f_{25} color ratios for each source. We have also compiled f_{60}/f_{25} color ratios from *IRAS* for comparison, which probe much larger scales than our torus SEDs. Out of 21 sources, we obtained 17 *IRAS* f_{60}/f_{25} colors with good quality of fluxes (FQUAL = 3, which is the highest quality)⁵.

Figure 5 shows the relationship between the f_{60}/f_{25} flux ratios obtained from *IRAS* and those from the torus model SEDs. The averages *IRAS* f_{60}/f_{25} flux ratio for type-1, HBLR, and NHBLR AGN are 4.1 ± 2.5 , 3.7 ± 2.0 and 6.4 ± 2.4 , respectively, showing the previously mentioned correlation for HBLR and NHBLR AGN, although with large error bars. However, when we compare the values obtained from the torus model SEDs, which exclude contamination from the host galaxy, we find that they are very similar for the three groups and smaller than the *IRAS* colors ($f_{60}/f_{25} = 0.63 \pm 0.07$, 0.80 ± 0.48 , and 0.75 ± 0.18 for type-1, HBLR, and NHBLR AGN respectively).

These results show that the differences of *IRAS* f_{60}/f_{25} among the three subgroups are not produced from the torus dust. A similar result was reported by Alexander (2001), but using X-ray observations. Although the standard deviations of the average values of the *IRAS* colors are large for the three subgroups, one possible explanation for the cooler *IRAS* colors of NHBLR in comparison with those of HBLR AGN could be dust emission from stronger starbursts in their host galaxies. This is in good agreement with previous results showing that highly obscured AGN tend to have higher star formation activity in their host galaxies (Goulding et al. 2012; Ichikawa et al. 2012a,b, 2014; Castro et al. 2014). Therefore, larger obscuration from the torus in NHBLR AGN (as shown in Figure 4) and higher star formation activity in the host galaxy could be somehow coupled. For example, using three-dimensional hydrodynamical simulations, Wada & Norman (2002) showed that starbursts and supernovae within the central 100 pc of host galaxies help lifting up the torus, suggesting that high star formation activity could influence the scale height of the torus. Comparing the nuclear and overall star formation activity of AGN with the torus obscuration is crucial to find out if they are coupled (e.g., Imanishi et al. 2011; Esquej et al. 2014; Ichikawa et al. 2014).

5. CONCLUSIONS

We constructed 21 infrared torus-dominated SEDs including high spatial resolution NIR and MIR photometry, MIR spectroscopy, and *Spitzer* and *Herschel* FIR fluxes. By performing SED fitting using clumpy torus models and a Bayesian approach we derived torus parameters such as the torus covering factor (C_T), the torus inner and outer radius (r_{in} and r_{out}), and the torus scale height (H). We divided the sample into subgroups based on whether or not they are optically type-1, type-2 with observational hidden broad line regions sign (HBLR), and type-2 without any observational broad line region signs (NHBLR). Our results are summarized as follows:

1. Under the assumption of a clumpy distribution of

⁵ See Beichman et al. (1988) for the definition of FQUAL in the *IRAS* catalogs. False detections may be included when FQUAL < 3.

the dust, we obtained a quantitative description of the torus geometry and intrinsic properties. We found that the median torus outer radius for the whole sample $r_{\text{out}} = 1.2$ pc is consistent with the results from MIR interferometry observations.

2. We found that the tori of Type-1 AGN have smaller σ , Y , N_{H} , and C_{T} than those of HBLR and NHBLR. Moreover, the tori of NHBLR are thicker and therefore have higher C_{T} than those of HBLR. These differences in the torus properties of HBLR and NHBLR AGN would make it more difficult to detect hidden BLR in NHBLR.
3. Combining f_{60}/f_{25} colors obtained from *IRAS* photometry and from torus model SEDs, we showed that the low f_{60}/f_{25} measured for HBLR using *IRAS* data are not due to a more face-on inclination of torus, but rather to star formation activity in their host galaxies.

We are grateful for useful comments from the anonymous referee. We also thank C. Ricci, M. Stalevski for useful comments and discussions. K.I. thanks the Department of Physics and Astronomy at University of Texas at San Antonio, where most of the research was conducted. This paper is based on observations obtained at the Gemini Observatory, which is operated by the Association of Universities for Research in Astronomy, Inc., under a cooperative agreement with the NSF on behalf of the Gemini partnership. This work was partly supported by the Grant-in-Aid for JSPS Fellows for young researchers (K.I.). C.P. acknowledges support from UTSA and NSF (grant number 0904421). C.R.A. is supported by a Marie Curie Intra European Fellowship within the 7th European Community Framework Programme (PIEF-GA-2012-327934). A.A.-H. acknowledges support from the Spanish Plan Nacional de Astronomía y Astrofísica under grant AYA2012-31447.

REFERENCES

- Alexander, D. M., Hough, J. H., Young, S., et al. 1999, *MNRAS*, 303, L17
- Alexander, D. M. 2001, *MNRAS*, 320, L15
- Alonso-Herrero, A., Quillen, A. C., Rieke, G. H., Ivanov, V. D., & Efstathiou, A. 2003, *AJ*, 126, 81
- Alonso-Herrero, A., Ramos Almeida, C., Mason, R., et al. 2011, *ApJ*, 736, 82
- Alonso-Herrero, A., Sánchez-Portal, M., Ramos Almeida, C., et al. 2012, *MNRAS*, 425, 311
- Alonso-Herrero, A., Pereira-Santaella, M., Rieke, G. H., & Rigopoulou, D. 2012, *ApJ*, 744, 2
- Antonucci, R. R. J., & Miller, J. S. 1985, *ApJ*, 297, 621
- Antonucci, R. 1993, *ARA&A*, 31, 473
- Asensio Ramos, A., & Ramos Almeida, C. 2009, *ApJ*, 696, 2075
- Asmus, D., Gandhi, P., Smette, A., Hönig, S. F., & Duschl, W. J. 2011, *A&A*, 536, A36
- Baumgartner, W. H., Tueller, J., Markwardt, C. B., et al. 2013, *ApJS*, 207, 19
- Beichman, C. A., Neugebauer, G., Habing, H. J., Clegg, P. E., & Chester, T. J. 1988, *Infrared astronomical satellite (IRAS) catalogs and atlases. Volume 1: Explanatory supplement*, 1
- Blanco, P. R., Ward, M. J., & Wright, G. S. 1990, *MNRAS*, 242, 4P
- Brightman, M., & Nandra, K. 2011, *MNRAS*, 413, 1206
- Brewer, B. J., Elliott, T. M. 2014, *MNRAS*, 439, L31
- Carollo, C. M., Stiavelli, M., Seigar, M., de Zeeuw, P. T., & Dejonghe, H. 2002, *AJ*, 123, 159
- Castro, A., Miyaji, T., Shirahata, M., et al. 2014, arXiv:1408.3172
- Deo, R. P., Richards, G. T., Crenshaw, D. M., & Kraemer, S. B. 2009, *ApJ*, 705, 14
- Efstathiou, A., & Rowan-Robinson, M. 1995, *MNRAS*, 273, 649
- Elitzur, M. 2012, *ApJ*, 747, L33
- Elitzur, M., Ho, L. C., & Trump, J. R. 2014, *MNRAS*, 438, 3340
- Elvis, M., Wilkes, B. J., McDowell, J. C., et al. 1994, *ApJS*, 95, 1
- Esquej, P., Alonso-Herrero, A., González-Martín, O., et al. 2014, *ApJ*, 780, 86
- Feltre, A., Hatziminaoglou, E., Fritz, J., & Franceschini, A. 2012, *MNRAS*, 426, 120
- Galliano, E., & Alloin, D. 2008, *A&A*, 487, 519
- Gandhi, P., Horst, H., Smette, A., et al. 2009, *A&A*, 502, 457
- García-Burillo, S., Combes, F., Usero, A., et al. 2014, *A&A*, 567, A125
- González-Martín, O., Rodríguez-Espinosa, J. M., Díaz-Santos, T., et al. 2013, *A&A*, 553, A35
- Goulding, A. D., Alexander, D. M., Bauer, F. E., et al. 2012, *ApJ*, 755, 5
- Gu, Q., Maiolino, R., & Dultzin-Hacyan, D. 2001, *A&A*, 366, 765
- Guainazzi, M., Rodríguez-Pascual, P., Fabian, A. C., Iwasawa, K., & Matt, G. 2004, *MNRAS*, 355, 297
- Heisler, C. A., Lumsden, S. L., & Bailey, J. A. 1997, *Nature*, 385, 700
- Ho, L. C., Filippenko, A. V., & Sargent, W. L. W. 1997, *ApJS*, 112, 315
- Hönig, S. F., Beckert, T., Ohnaka, K., & Weigelt, G. 2006, *A&A*, 452, 459
- Hönig, S. F., & Kishimoto, M. 2010, *A&A*, 523, A27
- Hönig, S. F., Leipski, C., Antonucci, R., & Haas, M. 2011, *ApJ*, 736, 26
- Hönig, S. F., Gandhi, P., Asmus, D., et al. 2014, *MNRAS*, 438, 647
- Ichikawa, K., Ueda, Y., Terashima, Y., et al. 2012, *ApJ*, 754, 45
- Ichikawa, K., Ueda, Y., Terashima, Y., et al. 2012, *Torus Workshop*, 2012, 109
- Ichikawa, K., Imanishi, M., Ueda, Y., et al. 2014, *ApJ*, 794, 139
- Imanishi, M. 2002, *ApJ*, 569, 44
- Imanishi, M., Ichikawa, K., Takeuchi, T., et al. 2011, *PASJ*, 63, 447
- Itoh, T., Done, C., Makishima, K., et al. 2008, *PASJ*, 60, 251
- Jiménez-Bailón, E., Santos-Lleó, M., Dahlem, M., et al. 2005, *A&A*, 442, 861
- Kawaguchi, T., & Mori, M. 2010, *ApJ*, 724, L183
- Kawaguchi, T., & Mori, M. 2011, *ApJ*, 737, 105
- Kishimoto, M., Hönig, S. F., Beckert, T., & Weigelt, G. 2007, *A&A*, 476, 713
- Kishimoto, M., Hönig, S. F., Antonucci, R., et al. 2009, *A&A*, 507, L57
- Kishimoto, M., Hönig, S. F., Antonucci, R., et al. 2011, *A&A*, 536, 78
- Koshida, S., Yoshii, Y., Kobayashi, Y., et al. 2009, *ApJ*, 700, L109
- Kullback, S., & Leibler, A. 1951, *Ann. Math. Stat.*, 22, 79
- Lawrence, A. 1991, *MNRAS*, 252, 586
- Levenson, N. A., Heckman, T. M., Krolik, J. H., Weaver, K. A., & Zdotycki, P. T. 2006, *ApJ*, 648, 111
- Lira, P., Videla, L., Wu, Y., et al. 2013, *ApJ*, 764, 159
- Lumsden, S. L., Heisler, C. A., Bailey, J. A., Hough, J. H., & Young, S. 2001, *MNRAS*, 327, 459
- Lumsden, S. L., Alexander, D. M., & Hough, J. H. 2004, *MNRAS*, 348, 1451
- Maiolino, R., & Rieke, G. H. 1995, *ApJ*, 454, 95
- Marin, F. 2014, *MNRAS*, 441, 551
- Marinucci, A., Bianchi, S., Nicastro, F., Matt, G., & Goulding, A. D. 2012, *ApJ*, 748, 130
- Meisenheimer, K., Tristram, K. R. W., Jaffe, W., et al. 2007, *A&A*, 471, 453
- Meléndez, M., Mushotzky, R. F., Shimizu, T. T., Barger, A. J., & Cowie, L. L. 2014, *ApJ*, 794, 152
- Miller, J. S., & Goodrich, R. W. 1990, *ApJ*, 355, 456
- Mor, R., & Trakhtenbrot, B. 2011, *ApJ*, 737, L36
- Mor, R., & Netzer, H. 2012, *MNRAS*, 420, 526
- Moran, E. C., Barth, A. J., Kay, L. E., & Filippenko, A. V. 2000, *ApJ*, 540, L73
- Moran, E. C., Kay, L. E., Davis, M., Filippenko, A. V., & Barth, A. J. 2001, *ApJ*, 556, L75
- Moran, E. C., Filippenko, A. V., & Chornock, R. 2002, *ApJ*, 579, L71
- Nagar, N. M., Oliva, E., Marconi, A., Maiolino, R. 2002, *A&A*, 391, L21
- Neenkova, M., Ivezić, Ž., & Elitzur, M. 2002, *ApJ*, 570, L9
- Neenkova, M., Sirocky, M. M., Ivezić, Ž., & Elitzur, M. 2008, *ApJ*, 685, 147
- Neenkova, M., Sirocky, M. M., Nikutta, R., Ivezić, Ž., & Elitzur, M. 2008, *ApJ*, 685, 160

- Nenkova, M., Sirocky, M. M., Nikutta, R., Ivezić, Ž., & Elitzur, M. 2010, *ApJ*, 723, 1827
- Netzer, H., Lira, P., Trakhtenbrot, B., Shemmer, O., & Cury, I. 2007, *ApJ*, 671, 1256
- Nicastro, F., Martocchia, A., & Matt, G. 2003, *ApJ*, 589, L13
- Nikutta, R., Elitzur, M., & Lacy, M. 2009, *ApJ*, 707, 1550
- Ossenkopf, V., Henning, T., & Mathis, J. S. 1992, *A&A*, 261, 567
- Peng, Z., Gu, Q., Melnick, J., & Zhao, Y. 2006, *A&A*, 453, 863
- Pier, E. A., & Krolik, J. H. 1992, *ApJ*, 401, 99
- Pier, E. A., & Krolik, J. H. 1993, *ApJ*, 418, 673
- Polletta, M., Weedman, D., Hönig, S., et al. 2008, *ApJ*, 675, 960
- Quillen, A. C., McDonald, C., Alonso-Herrero, A., et al. 2001, *ApJ*, 547, 129
- Ramos Almeida, C., Pérez García, A. M., Acosta-Pulido, J. A., González-Martín, O. 2008, *ApJ*, 680, L17
- Ramos Almeida, C., Levenson, N. A., Rodríguez Espinosa, J. M., et al. 2009, *ApJ*, 702, 1127
- Ramos Almeida, C., Levenson, N. A., Alonso-Herrero, A., et al. 2011, *ApJ*, 731, 92
- Ramos Almeida, C., Sánchez-Portal, M., Pérez García, A. M., et al. 2011, *MNRAS*, 417, L46
- Ramos Almeida, C., Alonso-Herrero, A., Levenson, N. A., et al. 2014, *MNRAS*, 439, 3847
- Reunanen, J., Kotilainen, J. K., & Prieto, M. A. 2003, *MNRAS*, 343, 192
- Ricci, C., Walter, R., Courvoisier, T. J.-L., & Paltani, S. 2011, *A&A*, 532, A102
- Ricci, C., Paltani, S., Awaki, H., et al. 2013, *A&A*, 553, A29
- Ricci, C., Ueda, Y., Ichikawa, K., et al. 2014, *A&A*, 567, A142
- Scarrott, S. M., Draper, P. W., Stockdale, D. P., & Wolstencroft, R. D. 1993, *MNRAS*, 264, L7
- Schartmann, M., Meisenheimer, K., Camenzind, M., et al. 2008, *A&A*, 482, 67
- Schmitt, H. R. 2001, *AJ*, 122, 2243
- Simpson, C. 1998, *ApJ*, 509, 653
- Stalevski, M., Fritz, J., Baes, M., Nakos, T., Popovic, L. 2012, *MNRAS*, 240, 2756
- Tran, H. D. 2001, *ApJ*, 554, L19
- Tran, H. D. 2003, *ApJ*, 583, 632
- Tran, H. D. 2010, *ApJ*, 711, 1174
- Tran, H. D., Lyke, J. E., & Mader, J. A. 2011, *ApJ*, 726, L21
- Tueller, J., Mushotzky, R. F., Barthelmy, S., et al. 2008, *ApJ*, 681, 113
- Véron-Cetty, M.-P., & Véron, P. 2006, *A&A*, 455, 773
- Wada, K., & Norman, C. A. 2002, *ApJ*, 566, L21
- Wang, J.-M., & Zhang, E.-P. 2007, *ApJ*, 660, 1072